Final Report

NASA NRA-99-GRC-2

NASA NAG 32311

Investigation of Conjugate Heat Transfer in Turbine Blades and Vanes

By

Kassab, A.J. and Kapat, J.S.

Mechanical, Materials, and Aerospace Engineering
University of Central Florida
Orlando, Florida 32816-2450
Tel: 407-823-5778
Fax: 407-823-0208
Email: kassab@mail.ucf.edu

Abstract

We report on work carried out to develop a 3-D coupled Finite Volume/BEM-based temperature forward/flux back (TFFB) coupling algorithm to solve the conjugate heat transfer (CHT) which arises naturally in analysis of systems exposed to a convective environment. Here, heat conduction within a structure is coupled to heat transfer to the external fluid which is convecting heat into or out of the solid structure. There are two basic approaches to solving coupled fluid-structural systems. The first is a direct coupling where the solution of the different fields is solved simultaneously in one large set of equations. The second approach is a loose coupling strategy where each set of field equations is solved to provide boundary conditions for the other. The equations are solved in turn until an iterated convergence criterion is met at the fluid-solid interface. The loose coupling strategy is particularly attractive when coupling auxiliary field equations to computational fluid dynamics codes. We adopt the latter method in which the BEM is used to solve heat conduction inside a structure which is exposed to a convective field which in turn is resolved by solving the NASA Glenn compressible Navier-Stokes finite volume code Glenn-HT. The BEM code features constant and bi-linear discontinuous elements and an ILU-preconditioned GMRES iterative solver for the resulting non-symmetric algebraic set arising in the conduction solution. Interface of flux and temperature is enforced at the solid/fluid interface, and a radial-basis function scheme is used to interpolated information between the CFD and BEM surface girds. Additionally, relaxation is implemented in passing the fluxes from the condution solution to the fluid solution. Results from a simple test example are reported.

1 Introduction

As field solvers have matured, coupled field analysis has received much attention in an effort to obtain computational models ever-more faithful to the physics being modeled, see for instance [1]. The coupled field problem which we address is the conjugate heat transfer (CHT) problem arising commonly in practice: time dependent or time independent convective heat transfer over coupled to conduction heat transfer within a solid body, see Fig. (1). Examples of CHT include analysis of automotive engine blocks, fuel ejectors, cooled turbine blade/vanes, nozzle or combustor walls, or thermal protection system for re-entry vehicles. Applications of interest are then any thermal system in which multi-mode convective/conduction heat transfer is of particular importance to thermal design, and thus CHT arises naturally in most instances where external and internal temperature fields are coupled.

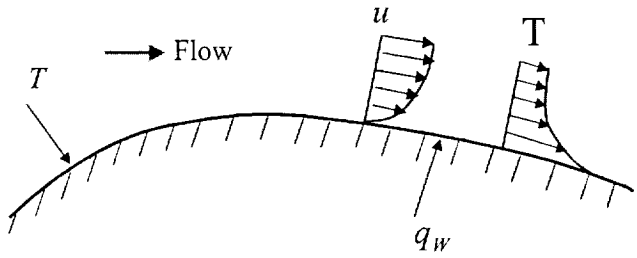

Figure 1: CHT problem: external convective heat transfer coupled to heat conduction within the solid.

However, conjugacy is often ignored in numerical simulations. For instance, in analysis of turbomachinery, separate flow and thermal analyses are typically performed, and, a constant wall temperature or heat flux boundary condition is typically imposed for the flow solver. Convective heat transfer coefficients are then obtained from the flow solution, and these are provided to the conduction solver to determine the temperature field and eventually to perform further thermal stress analysis. The shortcomings of this approach which neglects the effects of the wall temperature distribution on the development of the thermal boundary layer are overcome by a CHT analysis in which the coupled nature of the field problem is explicitly taken into account in the analysis.

There are two basic approaches to solving coupled field problems. In the first approach, a direct coupling is implemented in which different fields are solved simultaneously in one large set of equations. Direct coupling is mostly applicable for problems where time accuracy is critical, for instance, in aero-elasticity applications where the time scale of the fluid motion is on the same order as the structural modal frequency. However, this approach suffers from a major disadvantage due to the mismatch in the structure of the coefficient matrices arising from BEM, FEM and/or FVM solvers. That is, given the fully populated nature of the BEM

coefficient matrix, the direct coupling approach would severely degrade numerical efficiency of the solution by directly incorporating the fully populated BEM equations into the sparsely banded FEM or FVM equations. A second approach which may be followed is a loose coupling strategy where each set of field equations is solved separately to produce boundary conditions for the other. The equations are solved in turn until an iterated convergence criterion, namely continuity of temperature and heat flux, is met at the fluid-solid interface. The loose coupling strategy is particularly attractive when coupling auxiliary field equations to computational fluid dynamics codes as the structure of neither solver interferes in the solution process.

There are several algorithmic approaches which can be taken to solve the coupled field problems. Most commonly used methods are based on either finite elements (FEM), finite volume methods (FVM), or a combination of these two field solvers. Examples of such loosely coupled approaches applied to a variety of CHT problems ranging from engine block models to turbomachinery can be found in Comini et al. [2], Shyy and Burke [3], Patankar [4], Kao and Liou [5], Hahn et al. [6], Bohn et al. [7], and in Tayla et al. [8] where multi-disciplinary optimization is considered for CHT modeled turbine airfoil designs. Hassan et al. [9] develop a conjugate algorithm which loosely couples a FVM-based Hypersonic CFD code to an FEM heat conduction solver in an effort to predict ablation profiles in hypersonic re-entry vehicles. Here, the structured grid of the flow solver is interfaced with the un-structured grid of heat conduction solvers in a quasi-transient CHT solution tracing the re-entry vehicle trajectory. Issues in loosely coupled analysis of the elastic response of solid structures perturbed by external flowfields arising in aero-elastic problems can be found in Brown [10]. In either case, the coupled field solution requires complete meshing of both fluid and solid regions while enforcing solid/fluid interface continuity of fluxes and temperatures, in the case of CHT analysis, or displacement and traction, in the case of aero-elasticity analysis.

A different approach taken by Li and Kassab [11,12] and Ye et al. [12] who develop a HCT algorithm which avoids meshing of the solid region to resolve the heat conduction problem. In particular, the method couples the boundary element method (BEM) to an FEM Navier-Stokes solver to solve a steady state compressible subsonic CHT problem over cooled and uncooled turbine blades. Due to the boundary-only discretization nature of the BEM, the onerous task of grid generation within intricate solid regions is avoided. Here, the boundary discretization utilized to generate the computational grid for the external flow-field provides the boundary discretization required for the boundary element method. In cases where the solid is multiply-connected, such as a cooled turbine blade, the interior boundary surfaces must also be discretized; however, this poses little additional effort. Moreover, in addition to eliminating meshing the solid region, this BEM/FVM method offers an additional advantage in solving CHT problems which arises from the fact that nodal unknowns which appear in the BEM are the

surface temperatures and heat fluxes. Consequently, solid/fluid interfacial heat fluxes which are required to enforce continuity in CHT problems are naturally provided by the BEM conduction analysis. This is in contrast to the domain meshing methods such as FVM and FEM where heat fluxes are computed in a post-processing stage by numerical differentiation. He et al. [14,15] adopted this approach in further studies of CHT in incompressible flow in ducts subjected to constant wall temperature and constant heat flux boundary conditions. Kontinos [16] also adopted the BEM/FVM coupling algorithm to solve the CHT over metallic thermal protection panels at the leading edge of the X-33 in a Mach 15 hypersonic flow regime. Rahaim and Kassab [17] and Rahaim et al. [18] adopt a BEM/FVM strategy to solve time-accurate CHT problems for supersonic compressible flow, and they present experimental validation of this CHT solver. In their studies, the dual reciprocity BEM [19] is used to for transient heat conduction, while a cell-centered FVM is chosen to resolve the compressible turbulent Navier-Stokes equations.

We now present work carried out under this grant which extends the loosely coupled BEM/FVM approach to solving CHT problems in steady state for 3-D problems. Here, we couple a 3-D BEM conduction solver with the NASA Glenn multi-block FVM Navier-Stokes convective heat transfer code, Glenn-HT. This density based FVM code is a robust and well-proven code developed specifically for fluid-flow and heat transfer analysis in turbomachinery applications. The methodology adopted in this work is given as well as the information passing process. Results are presented for a test-case configuration to be used in future laboratory experiments which will serve as experimental validation of the CHT solver.

2 Governing Equations

The governing equations for the mixed field problem under consideration are reviewed. The CHT problems arising in turbomachinery involves external flow fields that are generally compressible and turbulent, and these are governed by the compressible Navier-Stokes equations supplemented by a turbulence model. Heat transfer within the blade is governed by the heat conduction equation, and linear as well as non-linear options are considered. However, fluid flows within internal structures to the blade, such as film cooling holes and channels, are usually low-speed and incompressible. Consequently, density-based compressible codes are not directly applicable to modeling such flows, unless low Mach number pre-conditioning is implemented, see Turkel [25,26]. It is also noted that the Glenn-HT code is specialized to turbomachinery applications for which air is the working fluid and which is modeled as an ideal gas.

2.1 The Flow Field

The governing equations for the external fluid flow and heat transfer are the compressible Navier-Stokes equations, which describe the conservation of mass, momentum and energy. These can be written in integral form as

$$\frac{\partial}{\partial t}\int_{\Omega} \underset{\sim}{W}\, d\Omega + \int_{\Gamma} \underset{\sim}{F}\cdot\hat{n}\, d\Gamma - \int_{\Gamma} \underset{\sim}{T}\cdot\hat{n}\, d\Gamma = \int_{\Omega} \underset{\sim}{S}\, d\Omega \tag{1}$$

where Ω denotes the volume, Γ denotes the surface bounded by the volume Ω, and $\hat{n}$ is the outward-drawn normal. The conserved variables are contained in the vector $\underset{\sim}{W} = (\rho,\ \rho u,\ \rho v,\ \rho w,\ \rho e,\ \rho k,\ \rho\omega)$, where, $\rho,\ u,\ v,\ w,\ e,\ k, \omega$ are the density, the velocity components in x-, y-, and z-directions, and the specific total energy. k and ω are the kinetic energy of turbulent fluctuations and the specific dissipation rate of the two equation k-ω Wilcox turbulence model [23, 24] is adopted in Glenn-HT. The vectors $\underset{\sim}{F}$ and $\underset{\sim}{T}$ are convective and diffusive fluxes respectively, $\underset{\sim}{S}$ is a vector containing all terms arising from the use of a non-inertial reference frame as well as production and dissipation of turbulent quantities. The fluid is modeled as an ideal gas. A rotating frame of reference can be adopted for rotating flow studies. The effective viscosity is given by

$$\mu = \mu_l + \mu_t \tag{2}$$

where $\mu_t = \rho k/\omega$. The thermal conductivity of the fluid is then computed by a Prandtl number analogy where

$$k_f = \frac{\gamma}{\gamma - 1}\left[\frac{\mu_l}{Pr_l} + \frac{\mu_t}{Pr_t}\right] \tag{3}$$

and Pr is the Prandtl number and γ is the specific heat ratio. The subscribes l and t refers to laminar and turbulent values respectively.

2.2 The Heat Conduction Field

In the CHT model, the NS equations are solved to steady state by a time marching scheme. As physically realistic time-dependent solutions are not sought, a quasi-steady heat conduction analysis using the BEM is performed at a given time level. As such, only steady-state heat conduction is considered. The governing equation is

$$\nabla \cdot [k(T_s)\nabla T_s] = 0 \tag{4}$$

where, T_s denotes the temperature of the solid, and k_s is the thermal conductivity of the solid material. If the thermal conductivity is taken as constant, then the above reduces to the following equation for the temperature

$$k\nabla^2 T = 0 \tag{5}$$

When the thermal conductivity variation with temperature is an important concern, the nonlinearity of the heat conduction equation can readily be removed by introducing the classical Kirchhoff transform, $U(T)$, which is defined as

$$= \frac{}{o} \int_{T_o}^{T} s \tag{6}$$

where T_o is the reference temperature and k_o is the reference thermal conductivity. The transform and its inverse are readily evaluated, either analytically or numerically, and the heat conduction equation transforms to a Laplace equation for the transform parameter $U(T)$, that is the nonlinear heat conduction problem transforms to

$$k_o \nabla^2 U = 0 \tag{7}$$

and the boundary conditions of the first and second kind transform linearly as

$$U = U(T_s) \quad \text{and} \quad k_o \frac{\partial U}{\partial n} = k_s \frac{\partial T_s}{\partial n} \tag{8}$$

Thus, the nonlinear problem in T subjected to any combination of 1st or 2nd kind boundary conditions transforms to a linear problem in the transform parameter U. The heat conduction equation thus reduces to the Laplace equation in any case, and this equation is readily solved by the BEM.

In the conjugate problem, continuity of temperature and heat flux at the blade surface, Γ, must be satisfied:

$$\begin{aligned} T_f &= T_s \\ k_f \frac{\partial T_f}{\partial n} &= -k_s \frac{\partial T_s}{\partial n} \end{aligned} \tag{9}$$

Here, T_f is the temperature computed from the N-S solution, T_s is the temperature within the solid which is computed from the BEM solution, and $\partial/\partial n$ denotes the normal derivative. Both first kind and second kind boundary conditions transform linearly in the case of temperature dependent conductivity. As will be explained later, in such a case, the fluid temperature is used to evaluate the Kirchhoff transform and this is used a boundary condition of the first kind for the BEM conduction solution in the solid. Subsequently the computed heat flux, in terms of U, is scaled to provide the heat flux which is in turn used as an input boundary condition for the flow-field.

3 Field Solver Solution Algorithms

A brief description of the Glenn-HT code is given in this section. Details of the code and its verification can be found in [21,22]. The heat conduction equation is solved using BEM, and details are provided for this conduction solver.

3.1 Navier-Stokes Solver

A cell-centered FVM is used to discretize the NS equations. Eq. (1) is integrated over a hexahedral computational cell with the nodal unknowns located at the cell center (i, j, k). The

convective flux vector is discretized by a central difference supplemented by artificial dissipation as described in Jameson et al. [27]. The artificial dissipation is a blend of first and third order differences with the third order term active everywhere except at shocks and locations of strong pressure gradients. The viscous terms are evaluated using central differences. The resulting finite volume equations can be written as

$$V_{i,j,k}\frac{d\underset{\sim}{\overline{W}}_{i,j,k}}{dt}+\underset{\sim}{q}_{i,j,k}-\underset{\sim}{d}_{i,j,k}=\underset{\sim}{s}_{i,j,k} \tag{10}$$

where $\underset{\sim}{\overline{W}}_{i,j,k}$ is the cell-volume averaged vector of conserved variables, $\underset{\sim}{q}_{i,j,k}$ and $\underset{\sim}{d}_{i,j,k}$ are the net flux and dissipation for the finite volume obtained by surface integration of Eq. (1), and $\underset{\sim}{s}_{i,j,k}$ is the net finite source term. The above is solved using a time marching scheme based on a fourth order explicit Runge-Kutta time stepping algorithm. The steady-state solution is sought by marching in time until the dependent variables reach their steady-state values, and, as such, intermediate temporal solutions are not physically meaningful. In this mode of solving the steady-state problem, time-marching can be viewed as a relaxation scheme, and local time-stepping and implicit residual smoothing are used to accelerate convergence. A multi-grid option is available in the code, although it was not used in the results reported herein.

3.2 Heat Conduction Boundary Element Solution

The heat conduction equation reduces to the same governing Laplace equation in the temperature or the Kirchhoff transform. In the boundary element method this governing partial differential equation is converted into a boundary integral equation (BIE), see[28-31], as

$$C(\xi)\,T(\xi)+\int_S T(x)q^*(x,\xi)dS(x)=\int_S q(x)T^*(x,\xi)dS(x) \tag{11}$$

where $S(x)$ is the surface bounding the domain of interest, ξ is the source point, x is the field point, $q(x) = -k\partial T/\partial n$ is the heat flux, $T^*(x,\xi)$ is the so-called fundamental solution, and $q^*(x,\xi)$ is its normal derivative with $\partial/\partial n$ denoting the normal derivative with respect to the outward-drawn normal. The fundamental solution (or Green free space solution) is the response of the adjoint governing differential operator at any field point x due to a perturbation of a Dirac delta function acting at the source point ξ. In our case, since the steady state heat conduction equation is self-adjoint, we have

$$k\nabla^2 T^*(x,\xi) = -\delta(x,\xi) \tag{12}$$

Solution to this equation can be found by several means, see for instance Liggett and Liu [32], Morse and Feschbach [33], and Kellog [34], as

$$T^*(x,\xi) = -\frac{1}{2\pi k} ln\, r(x,\xi) \text{ in 2-D} \qquad (13)$$
$$= \frac{1}{4\pi k\, r(x,\xi)} \qquad \text{in 3-D}$$

where $r(x,\xi)$ is the Euclidean distance from the source point ξ. The free term $C(\xi)$ can be shown analytically to be

$$C(\xi) = \oint_{S(x)} -k \frac{\partial T^*(x,\xi)}{\partial n} dS(x) \qquad (14)$$

Moreover, introducing the definition of the fundamental solution in the above, it can be readily be determined that $C(\xi)$ is the internal angle (in degrees in 2-D and in steradians in 3-D) subtended at source point divided by 2π in 2-D and by 4π in 3-D when the source point ξ is on the boundary and takes on a value of one when the source point ξ is at the interior. Consequently, the free term takes on values $1 \geq C(\xi) \geq 0$.

In the BEM, the BIE is discretized using two levels of discretization:

1. the surface S is discretized into a series of $e = 1,2...N$ elements. This is traditionally accomplished using polynomial interpolation, bilinear and quadratic being the most common. In general,

$$S = \sum_{e=1}^{N} \Delta S^e \qquad (15)$$

and on each surface element S^e the geometry is discretized using local shape functions $N_k^e(\eta,\zeta)$ in terms a homogenous coordinates (η,ζ) which each take on values between $[-1,1]$ as

$$x^e(\eta,\zeta) = \sum_{k=1}^{NGE} N_k^e(\eta,\zeta) x_k \qquad (16)$$
$$y^e(\eta,\zeta) = \sum_{k=1}^{NGE} N_k^e(\eta,\zeta) y_k$$
$$z^e(\eta,\zeta) = \sum_{k=1}^{NGE} N_k^e(\eta,\zeta) z_k$$

Here, (x_k, y_k, z_k) denote the location of the $k = 1, 2...NGE$ boundary nodes used to define the element geometry.

2. the distribution of the temperature and heat flux is modeled on the surface. This is usually accomplished using polynomial interpoaltion as well. Common discretizations

include: constant (where the mean value of T and q) are taken on an element surface, blinear, or bi-quadratic. In general,

$$T^e(\eta,\zeta) = \sum_{j=1}^{NPE} N_j^e(\eta,\zeta) T_j^e \tag{17}$$
$$q^e(\eta,\zeta) = \sum_{j=1}^{NPE} N_j^e(\eta,\zeta) q_j^e$$

It is noted that the order of discretization of the temperature and heat flux need not be the same as that used for the geometry, leading to sub-parametric (lower order than that used for the geometry), iso-parametric (lower order than that used for the geometry), and super-parametric (lower order than that used for the geometry) discretizations. Moreover, the temperature and heat flux are discretized using $j = 1, 2, ...NPE$ discrete nodal values whose location within the element e can be chosen to

(a) coincide with the location of the geometric nodes: continuous elements.
(b) be located offset from the geometric nodes: discontinuous elements.

We choose to employ bi-linear discontinuous elements as they provide high levels of accuracy in computed heat flux values especially at sharp corners regions where first kind boundary conditions are imposed without resorting to special treatment of corner points required by continuous elements[30]. Such corner regions are often encountered in industrial problems and first kind boundary conditions are imposed there in the CHT algorithm to be shortly described. Moreover, the use of discontiuous elements throughout the BEM model eliminates much of tyhe overhead associated with continuous elements, in particular, there is no need to generate, store, or access a connectivity matrix when using discontinuous elements. Details of the discretization employed in the BEM code are provided in the Appendix.

Following standard BEM discretization the BIE leads to the following

$$C(\xi)\,T(\xi) = \sum_{e=1}^{N}\sum_{j=1}^{NPE} T_j^e \int\int_{\Delta S_j} q^*(x,\xi) dS^e - \sum_{e=1}^{N}\sum_{j=1}^{NPE} q_j^e \int\int_{\Delta S_j} T^*(x,\xi) dS^e \tag{18}$$

The surface integrals in the above equation depend purely on the local geometry of the element and the location ofthe source point ξ. These are evaluated numerically using Gauss quadratures. Upon collocation of the above at every boundary node where the temperature and heat flux are define, the following algebraic form is obtained:

$$[H]\{T_s\} = [G]\{q_s\} \tag{19}$$

Here the influence matrices [H] and [G] are evaluated numerically using quadratures. Details of the numerics are provided in the Appendix. These are solved subject to either of the following boundary conditions:

(a) at the external bounding wall: $T_s|_{\Gamma_e} = T_f$ (20)

(b) at internal cooling hole surfaces: $-k_s \frac{\partial T_s}{\partial n}|_{\Gamma_c} = h[\,T_s - T_\infty\,]|_{\Gamma_c}$ (21)

Here, T is the wall temperature computed from the N-S solution, T_s is the wall temperature computed from the BEM conduction solution, the external boundary is denoted by Γ_e, while Γ_c denotes the convective internal cooling hole boundaries. At this point the Glenn-HT code does not have low Mach number capabilities. As such, modeling of convection in the cooling passages must be accomplished using correlations and not simulated using the NS solver (although this is perfectly possible and would be consistent with the CHT philosophy with proper extensions of the NS solver). In addition, in certain cases, a full CHT model is not practical in the design stage. For instance, modeling of cooling passages in a turbine blade with intricate cooling schemes such as jet impingement cooling or turbulence enhancing ribs pose a serious computational challenge, and these are often better modeled using correlation equations. Consequently, a partial CHT model can be carried out with internal bounding walls modelled using the standard convective boundary condition at internal cooling hole surfaces.

The advantage of the BEM formulation over finite difference or finite element formulations is that no interior mesh is generated and the surface heat flux is computed in the solution. A GMRES iterative solver with an ILU pre-conditioning is used to solve the BEM equations.

3.3 CHT Algorithm

The Navier-Stokes equations for the external fluid flow and the heat conduction equation for heat conduction within the solid are interactively solved to steady state through a time-marching algorithm. The surface temperature obtained from the solution of the Navier-Stokes equations is used as the boundary condition of the boundary element method for the calculation of heat flux through the solid surface. This heat flux is in turn used as a boundary condition for the Navier-Stokes equations in the next time step. This procedure is repeated until a steady-state solution is obtained. In practice, the BEM is solved every few cycles of the FVM, say every two hundred, to update the boundary conditions, as intermediate solutions are not physical in this scheme. This is referred to as the temperature forward/flux back (TFFB) coupling algorithm as outlined below:

• FVM Navier-Stokes solver:

1. Begins with initial adiabatic boundary condition at solid surface.
2. Solves compressible NS for fluid region.
3. Provides temperature distribution to BEM conduction solver after a number of iterations.
4. Receives flux boundary condition from the BEM as input for next set of iterations.

• BEM conduction solver:

1. Receives temperature distribution from FVM solver.
2. Solves steady-state conduction problem.
3. Provides flux distribution to FVM solver.

The transfer of heat flux from the BEM to the FVM solver is accomplished after under-relaxation.

$$q = \beta\, q_{old}^{BEM} + (1-\beta) q_{new}^{BEM} \tag{22}$$

with β taken as 0.2 in all reported calculations. The choice of the relaxation parameter is through trial and error. In certain cases, it has been our experience that a choice of larger relaxation parameter can lead to non-convergent solutions[35]. The process is continued until the NS solver converges and wall temperatures and heat fluxes converge, that is until Eq. (23) is satisfied within a set tolerance

$$\begin{aligned} \| \underset{\sim}{T}_f - \underset{\sim}{T}_s \| &< \epsilon_T \\ \| \underset{\sim}{q}_f - \underset{\sim}{q}_s \| &< \epsilon_q \end{aligned} \tag{23}$$

where ϵ_T and ϵ_q are taken as 0.001.

It should be noted that alternatively, the flux may be specified as a boundary condition for the BEM code leading to a flux forward temperature back (FFTB) approach. However, when a fully conjugate solution is undertaken, this would amount to specifying second kind boundary conditions completely around the surface of a domain governed by an elliptic equation, resulting in a non-unique solution. Thus, the TFFB algorithm avoids such a situation. A blend of the TFFB and FFTB may resolve this problem and is the subject of ongoing work. Results of these studies will be reported elsewhere.

3.4 Interpolation Between BEM and FVM Grids

A major issue in information transfer between CFD and BEM is the difference in the levels of discretization between the two meshes employed in a typical CHT simulation. Accurate

resolution of the boundary layer requires a FVM surface grid which is much too fine to be used directly in the BEM. A much coarser surface grid is typically generated for the BEM solution of the conduction problem. The disparity in meshes is illustrated for the test section considered in this paper, see Fig. (2): the FVM grid in Fig. (3) used for the external flow solution is obviously much finer than the coarser BEM grid in Fig. (4) which was used for internal conduction analysis. The disparity between the two grids requires a general interpolation of the surface temperature and heat flux between the two solvers as it is not possible in general to isolate a single BEM nodes and identify a set of nearest FVM nodes. Indeed in certain regions where the CFD mesh is very fine, a BEM node can readily be surrounded by tens or more FVM nodes.

Radial basis function (RBF) interpolation [19,20] can naturally be adopted for this purpose. Consider Fig. (5), here the location of a BEM node is identified on the right-hand-side by a star-like symbol. Let the position of the BEM node of interest be denoted by $\vec{r}$, then, the value of the temperature at that location is interpolated using RBF's with poles located at the position $\vec{r}_i$ of each of the FVM surface nodes lying within a sphere of radius R_{max} centered about $\vec{r}$

$$T(\vec{r}) = \sum_{i=1}^{NPS} \alpha_i f_i(r) \tag{24}$$

where, NPS is the total number of FVM nodes contained within the sphere, $r = |\vec{r} - \vec{r}_i|$ denotes the Euclidean distance, and $f_i(r)$ are radial basis functions. Here, we use the standard conic function

$$f(r) = 1 + r \tag{25}$$

Collocating Eq. (24) at all $i = 1, 2...NPS$ nodes of the finite volume mesh surrounding the BEM node of interest, the expansion coefficients are found by solving the equation

$$\underset{\sim}{T} = \underline{\underline{F}}\, \underset{\sim}{\alpha} \tag{26}$$

where $\underset{\sim}{T}$ is the vector of FVM computed wall temperatures, and the interpolant matrix $\underline{\underline{F}}$ is known from RBF theory to be well conditioned and readily inverted. In all calculations, the maximum radius R_{max} of the sphere is set to 5% of the maximum distance within the solid region. This limit may be adjusted to suit the problem at hand.

4 Numerical Results

We now report on a preliminary simulation used to verify our algorithm. A 3-D model is made of a 2-D configuration used in an experiment set up to simulate heat transfer conditions in a cooled turbine blade tip and investigate the importance of conjugacy, see Fig. 2. Heated air at 319.5K enters horizontally at the left end of the channel, flows over the simulated tip gap, and out the bottom of the channel. The block is made of stainless-steel ($k = 14.9\,W/mK$,

$\rho = 8.03\text{x}10^3 kg/m^3$, $c = 502.48\, J/kgK$) and is cooled by a laminar flow of water at $286K$. The film coefficient in the cooling channels is calculated as 536 W/m^2K. In this simulation, convective boundary conditions are used to model flow in the channel as a full external flow and internal flow CHT solution was not carried out, due to the fact that the CFD code is specialized for turbomachinery applications and can only model air as a working fluid. All walls not exposed to the flow are adiabatic. The height of inlet channel is $0.02m$, the height of the outlet channel is $0.0025m$, width of passage between block and wall is $0.005m$, the length of inlet channel up to block is $0.40315m$, the length of outlet channel measured from block to exit is $0.40615m$. Total pressure at inlet is atmospheric and the back pressure at exit is 0.92 x inlet total pressure (i.e., p/P_inlet = 0.92). A 3-D model was constructed to model the centerline of the block. Four finite volume cells were used to model the width and the surface grid at the block are shown in Figs. 3 and 4. The FVM mesh uses 1104 surface cells, with a total of 200,000 finite volume cells. The BEM surface grid used 946 uniformly spaced boundary elements. The CHT solution was run to reduce residuals in density to $1.0\text{x}10^{-6}$ and in energy to $1.0\text{x}10^{-9}$. Results for the CHT predicted block surface temperature, flow passage temperature and Mach number are displayed in Figs. 6 and 7. The Mach number in center of inlet channel is approximately 0.06, and typical Mach number in outlet channel is approximately 0.068 (variation over the height of the channel due to the flow over the block).

5 Conclusions

A combined FVM/BEM method has been developed to solve the conjugate problem in CHT analysis. As a boundary only grid is used by the BEM, the computational time for the heat conduction analysis is insignificant compared to the time used for the NS analysis. The proposed method produces realistic results without using arbitrary assumptions for the thermal condition at the conductor surface. In practice, turbomachinery components such as modern cooled turbine blades which often contain upwards of five hundred film cooling holes and intricate internal serpentine cooling passages with complex convective enhancement configurations such as turbulating trip strips, pose a real computational challenge to BEM modeling. It is proposed to extend the current work by implementing either fast multipole-accelerated BEM or adoption of iterative block solvers for the BEM in order to address large-scale problem.

6 References

[1] Kassab, A.J. and Aliabadi, M.H.(eds.), *Advances in Boundary Elements: Coupled Field Problems,* Computational Mechanics, Boston, 2001.

[2] Comini, G., Saro, O. and Manzan, M., A Physical Approach to Finite Element Modeling of Coupled Conduction and Convection, *Numerical Heat Transfer, Part. B.*, Vol. 24, pp. 243-261, 1993.

[3] Shyy, W. and Burke, J., Study of Iterative Characteristics of Convective Diffusive and Conjugate Heat Transfer Problems, *Numerical HeatTransfer, Part. B.*, Vol. 26, pp. 21-37, 1994.

[4] Patankar, S.,V., A NumericalMethod for Conduction in Composite Materials, Flow in Irregular Geometries and Conjugate Heat Transfer, *Proc. 6th. Int. Heat Transfer Conf.*, NRC Canada, and Hemisphere Pub. Co., New York, Vol. 3, pp. 297-302, 1978.

[5] Kao, K.H., and Liou, M.S., Application of Chimera/Unstructured Hybrid grids for Conjugate Heat Transfer, *AIAA Journal*, Vol. 35, No.9, pp. 1472-1478, 1997.

[6] Hahn, Z., Dennis, B., and Dulikravich, G., Simulateneous Prediction of External Flow-field and Temperature in Internally Cooled 3-D Turbine Blade Material, *IGTI Paper 2000-GT-253*, 2000.

[7] Bohn, D., Becker, V., Kusterer, K., Otsuki, Y., Sugimoto, T., and Tanaka, R., 3-D Internal Conjugate Calculations of a Convectively Cooled Turbine Blade with Serpentine-Shaped Ribbed Channels, *IGTI Paper 99-GT-220*, 1999.

[8] Tayala, S.S., Rajadas, J.N., and Chattopadyay, A., Multidisciplinary Optimization for Gas Turbine Airfoil Design, *Inverse Problems in Engineering*, Vol. 8, No. 3, pp. 283- 307, 2000.

[9] Hassan, B., Kuntz, D. and Potter, D.L., Coupled Fluid/Thermal Prediction of Ablating Hypersonic Vehicles, *AIAA Paper 98-0168,* 1998.

[10] Brown, S.A., Displacement Extrapolations for CFD+CSM Aeroelastic Analysis, *AIAA Paper 97-1090*, 1997.

[11] Li, H. and Kassab, A.J., Numerical Prediction of Fluid Flow and Heat Transfer in Turbine Blades with Internal Cooling, *AIAA/ASME Paper 94-2933.*

[12] Li, H. and Kassab, A.J., A Coupled FVM/BEM Solution to Conjugate Heat Transfer in Turbine Blades, *AIAA Paper 94-1981.*

[13] Ye, R., Kassab, A.J., and Li, H.J.,FVM/BEM Approach for the Solution of Nonlinear Conjugate Heat Transfer Problems, *Proc. BEM 20,* Kassab, A.J., Brebbia, C.A., and Chopra, M.B., (eds.), Orlando, Florida, August 19-21, 1998, pp. 679-689.

[14] He, M., Kassab, A.J., Bishop, P.J., and Minardi, A., A Coupled FDM/BEM Iterative Solution for the Conjugate Heat Transfer Problem in Thick-Walled Channels: Constant Temperature Imposed at the Outer Channel Wall, *Engineering Analysis*, Vol. 15, No.1, pp. 43-50, 1995.

[15] He, M., Bishop, P., Kassab, A.J., and Minardi, A., A Coupled FDM/BEM solution for the Conjugate Heat Transfer Problem, *Numerical Heat Transfer, Part B: Fundamentals,* Vol. 28, No. 2, pp.139-154, 1995.

[16] Kontinos, D., Coupled Thermal Analysis Method with Application to Metallic Thermal Protection Panels, *AIAA Journal of Thermophysics and Heat Transfer*, Vol.11, No.2, pp.173-181, 1997.

[17] Rahaim, C.P., Kassab, A.J. and Cavalleri, R., A Coupled Dual Reciprocity Boundary Element/Finite Volume Method for Transient Conjugate Heat Transfer, *AIAA Journal of Thermophysics and Heat Transfer*, Vol. 14, No. 1, pp. 27-38, 2000.

[18] Rahaim, C., Cavelleri, R.J. and Kassab, A.J., Computational Code For Conjugate Heat Transfer Problems: An Experimental Validation Effort, *AIAA Paper 97-2487,* 1997.

[19] Partridge, P.W., Brebbia, C.A. and Wrobel, L.C., *The Dual Reciprocity Boundary Element Method*, Computational Mechanics Publications, Southampton, 1992.

[20] Powell, M.J.D., The Theory of Radial Basis Function Approximation, *Advances in Numerical Analysis,* Vol. II, Light, W. (ed.), Oxford Science Publications, 1992.

[21] Steinthorsson, E., Ameri, A., and Rigby, D., *LeRC-HT -The NASA Lewis Research Center General Multi-Block Navier-Stokes Convective Heat Transfer Code*, (unpublished).

[22] Steinthorsson, E., Liou, M.-S, and Povinelli, L.A., Development of an Explicit Multi-block/Multigrid Flow Solver for Viscous Flows in Complex Geometries, *AIAA Paper 93-2380,* 1993.

[23] Wilcox, D.C., Turbulence Modeling for CFD, DCW Industries, La Canada, California, 1993.

[24] Wilcox, D.C., Simulation of transition with a two-equation turbulence model, *AIAA Journal*, Vol. 32, No. 2, pp. 247-255, 1994.

[25] Turkel, E., Preconditioned Methods for Solving the Incompressible and Low-Speed Compressible Equations, *Journal of Computational Physics*, Vol. 72, No. 2, pp. 277-298, 1987.

[26] Turkel, E., Review of Preconditioning Methods for Fluid Dynamics, *Applied Numerical Mathematics*, Vol. 12, pp. 257-284, 1993.

[27] Jameson,A., Schmidt,W., and Turkel,E., Numerical simulation of the Euler equations by the finite volume methods using Runge-Kutta time stepping schemes, *AIAA Paper 81-1259.*

[28] Brebbia, C.A., Telles, J.C.F. and Wrobel, L.C., *Boundary Element Techniques*, Springer-Verlag, Berlin, 1984.

[29] Brebbia, C.A. and Dominguez, J., *Boundary Elements: An Introductory Course*, Computational Mechanics Pub., Southampton and McGraw-Hill, New York,1989.

[30] Kane, J.H., *Boundary Element Analysis in Engineering Continuum Mechanics*, Prentice-Hall, New Jersey, 1993.

[31] Banerjee, P.K., *Boundary Element Method*, MacGraw Hill Book, Co, New York, 1994.

[32] Liggett, J.A., and Liu, P. L-F, *The Boundary Integral Equation Method for Porous Media Flow,*Allen & Unwin, Boston, 1983.

[33] Morse, P.M. and Feshbach, H., *Methods of Theoretical Physics*, McGraw-Hill, New York, 1953.

[34] Kellogg, O.D., *Foundations of Potential Theory*, Dover, New York, 1953.

[35] Bialecki, R., Ostrowski, Z., Kassab, A., Qi, Y., and Sciubba, E., Coupling Finite Element and Boundary Element Solutions, *Proc. of the 2001 European Conference on Computational Mechanics*, June 26-29, 2001, Cracow, Poland.

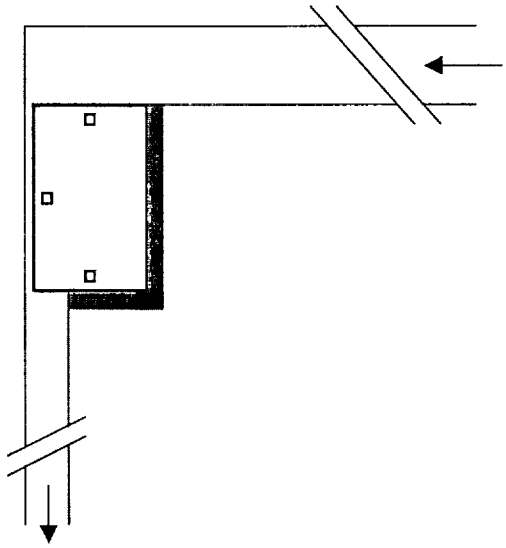

Figure 2: Cross-section of experiment set-up which is also used in numerical simulation. Upstream channel extends 10 hydraulic diameters upstream of the block.

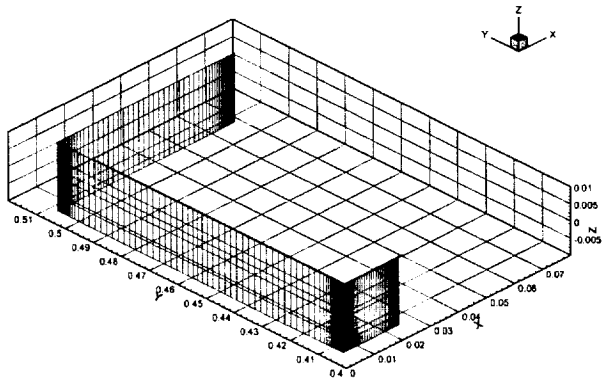

Figure 3: Finite Volume surface mesh: cell centered finite volumes with four cells in z-direction and total of 1104 surface cells.

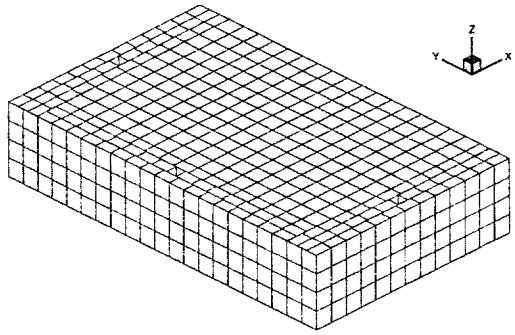

Figure 4: Surface BEM discretization for the block with 946 equally spaced bilinear elements distributed over the surface of the block.

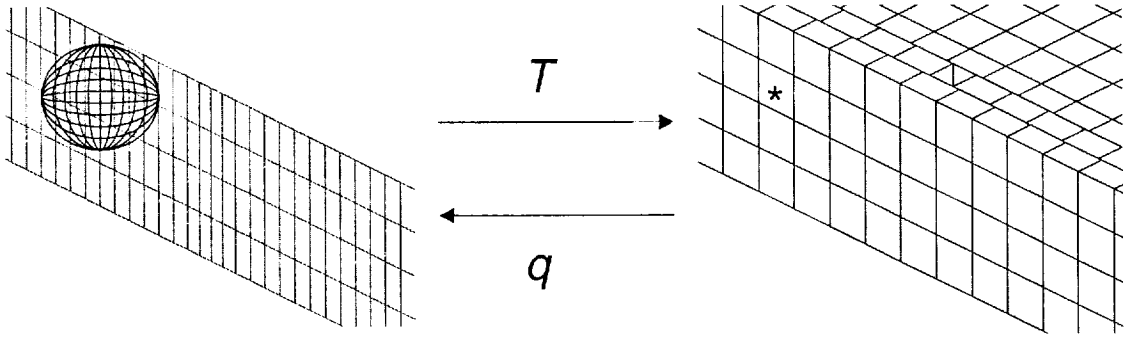

Figure 5: Transfer of nodal values from FVM and BEM (and back) independent surface meshes is performed with a compactly supported radial-basis-function interpolation.

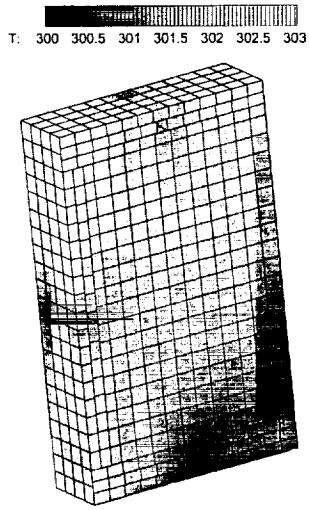

Figure 6: Surface temperature distribution from the converged conjugate solution (temperature distribution plotted from the BEM solution).

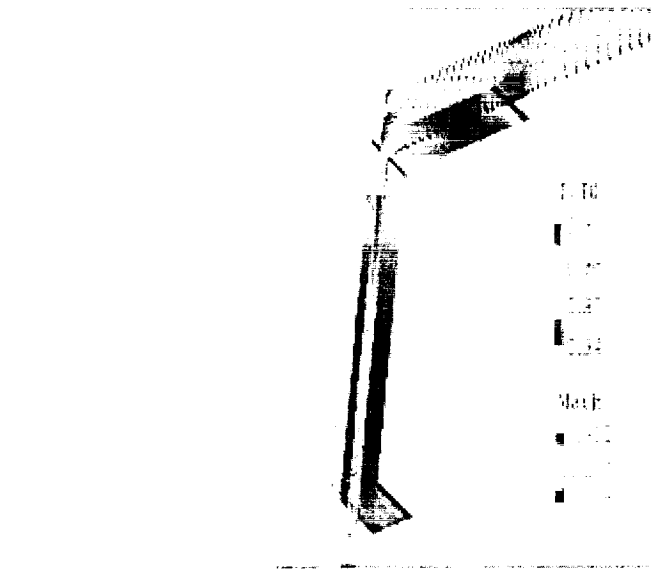

(a)

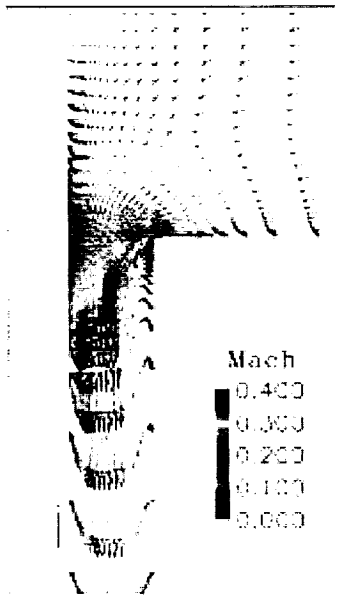

(b)

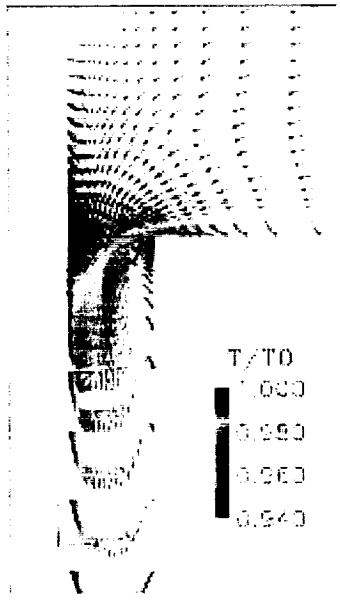

(c)

Figure 7: CHT predicted (a) flow passage temperatures and Mach numbers, (b) top corner Mach number, and (c) top corner temperatures.

APPENDIX

3D BEM FORMULATION FOR STEADY-STATE HEAT CONDUCTION

The point of departure is the BIE for the steady state heat conduction equation,

$$C(\xi)\,T(\xi)+\int_S T(x)q^*(x,\xi)dS(x)=\int_S q(x)T^*(x,\xi)dS(x) \tag{A.1}$$

where x denotes the 3-D coordinates, $S(x)$ is the surface bounding the domain of interest, ξ is the source point, x is the field point, $q(x) = -k\,\partial T/\partial n$ is the heat flux, $T^*(x,\xi)$ is the so-called fundamental solution, and $q^*(x,\xi)$ is its normal derivative with $\partial/\partial n$ denoting the normal derivative with respect to the outward-drawn normal. The fundamental solution (or Green free space solution) is the response of the adjoint governing differential operator at any field point x due to a perturbation of a Dirac delta function acting at the source point ξ. In our case, since the steady state heat conduction equation is self-adjoint, we have

$$k\nabla^2 T^*(x,\xi) = -\delta(x,\xi) \tag{A.2}$$

Solution to this equation can be found by several means which yield

$$\begin{aligned} T^*(x,\xi) &= -\frac{1}{2\pi k} ln\, r(x,\xi) \quad \text{in 2-D} \\ &= \frac{1}{4\pi k\, r(x,\xi)} \qquad \text{in 3-D} \end{aligned} \tag{A.3}$$

where $r(x,\xi) = |x-\xi|$ is the Euclidean distance from the source point ξ to the field point x. The free term $C(\xi)$ can be shown analytically to be

$$C(\xi) = \oint_{S(x)} -k\,\frac{\partial T^*(x,\xi)}{\partial n} dS \tag{A.4}$$

Moreover, introducing the definition of the fundamental solution in the above, it can be readily be determined that $C(\xi)$ is the internal angle (in degrees in 2-D and in steradians in 3-D) subtended at source point divided by 2π in 2-D and by 4π in 3-D when the source point ξ is on the boundary and takes on a value of one when the source point ξ is at the interior. Consequently, the free term takes on values $1 \geq C(\xi) \geq 0$.

In the BEM, the BIE is discretized using two levels of discretization:

1. the surface S is discretized into a series of $e = 1,2...N$ elements. This is traditionallyaccomplished using polynomial interpolation, bilinear and quadratic being the most common. In general,

$$S = \sum_{e=1}^{N} \Delta S^e \tag{A.5}$$

and on each surface element $\Delta S^e(x)$ the geometry is discretized using local shape functions $N_k^e(\eta, \zeta)$ in terms a homogenous coordinates (η, ζ) which each take on values between $[-1, 1]$ as

$$\begin{aligned} x^e(\eta,\zeta) &= \sum_{k=1}^{NGE} N_k^e(\eta,\zeta) x_k \\ y^e(\eta,\zeta) &= \sum_{k=1}^{NGE} N_k^e(\eta,\zeta) y_k \\ z^e(\eta,\zeta) &= \sum_{k=1}^{NGE} N_k^e(\eta,\zeta) z_k \end{aligned} \tag{A.6}$$

Here, (x_k, y_k, z_k) denote the location of the $k = 1, 2...NGE$ boundary nodes used to define the element geometry.

2. the distribution of the temperature and heat flux is modeled on the surface. This is usually accomplished using polynomial interpoaltion as well. Common discretizations include: constant (where the mean value of T and q) are taken on an element surface, blinear, or bi-quadratic. In general,

$$\begin{aligned} T^{\,e}(\eta,\zeta) &= \sum_{j=1}^{NE} N_j^e(\eta,\zeta) T_j^e \\ q^e(\eta,\zeta) &= \sum_{j=1}^{NE} N_j^e(\eta,\zeta) q_j^e \end{aligned} \tag{A.7}$$

It is noted that the order of discretization of the temperature and heat flux need not be the same as that used for the geometry, leading to sub-parametric (lower order than that used for the geometry) , iso-parametric (lower order than that used for the geometry), and super-parametric (lower order than that used for the geometry) discretizations. Moreover, the temperature and heat flux are

discretized using $j = 1, 2, ...NE$ discrete nodal values whose location within the element e can be chosen to

(a) coincide with the location of the geometric nodes: continuous elements.
(b) be located offset from the geometric nodes: discontinuous elements.

Two types of discontinuous boundary elements are available in the BEM code used in the project: constant elements (sub-parameteric) and bilinear isoparametric. All CHT calculations are reported using bi-linear discontinuous elements.

Constant Element

In the constant element, which is a sub-parametric element, the field variables, T and q, are modeled as constant across each element while the geometry is represented locally as bi-linear planes. Figure A.1 below shows a typical constant boundary element along with its transformed representation in the local $\eta - \zeta$ coordinate system.

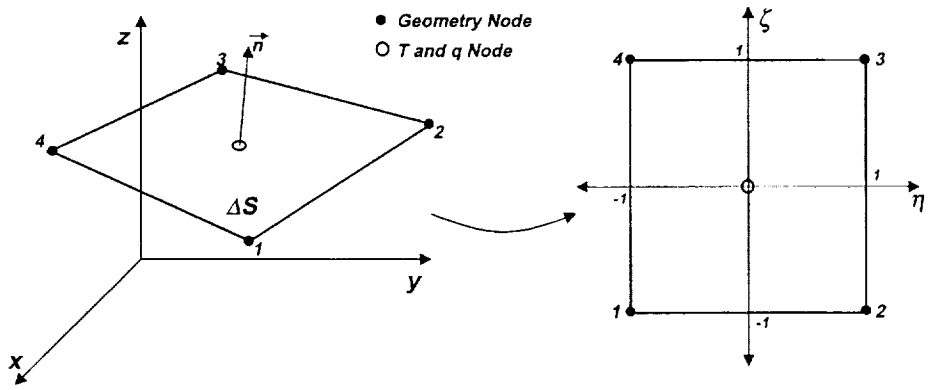

Figure A.1. Bi-linear subparametric boundary element.

Notice that the geometric nodal locations of the element are ordered counterclockwise such that the normal vector always points outwards from the domain of the problem. The global coordinate system (x, y, z) is transformed into a local coordinate system (η, ζ) using the following bi-linear shape functions relationships as,

$$x^e(\eta,\zeta) = \sum_{k=1}^{4} N_k^e(\eta,\zeta) x_k \tag{A.8}$$
$$y^e(\eta,\zeta) = \sum_{k=1}^{4} N_k^e(\eta,\zeta) y_k$$
$$z^e(\eta,\zeta) = \sum_{k=1}^{4} N_k^e(\eta,\zeta) z_k$$

where the four bi-linear shape functions are defined as follows,

$$N_1^e(\eta,\zeta) = \frac{1}{4}(1-\eta)(1-\zeta) \tag{A.9}$$
$$N_2^e(\eta,\zeta) = \frac{1}{4}(1+\eta)(1-\zeta)$$
$$N_3^e(\eta,\zeta) = \frac{1}{4}(1+\eta)(1+\zeta)$$
$$N_4^e(\eta,\zeta) = \frac{1}{4}(1-\eta)(1+\zeta)$$

The temperature and heat flux are modeled as constant with the node located at the geometric center of the boundary element, thus

$$T^e(\eta,\zeta) = T_j^e \quad \text{and} \quad q^e(\eta,\zeta) = q_j^e \tag{A.10}$$

Clearly, the temperature and heat flux are discontinuous at the element interfaces. Thus, a constant element is termed discontinuous.

Introducing the above discretization in the BIE in Eq. (A.1), noting that $NPE = 1$, and collocating the discretized BIE at each of the boundary nodes ξ_i there results

$$C(\xi_i)\, T(\xi_i) + \sum_{j=1}^{N} H_{ij} T_j = \sum_{j=1}^{N} G_{ij}\, q_j \tag{A.11}$$

where the influence coefficients H_{ij} and G_{ij} are defined as

$$H_{ij} = \int \int_{\Delta S_j} q^*(x,\xi_i)\, dS \tag{A.12}$$
$$G_{ij} = \int \int_{\Delta S_j} T^*(x,\xi_i)\, dS$$

These are evaluated numerically using Gauss-Legendre quadratures with an adaptive scheme to be discussed shortly. Although very simple in implementation, use of the the above constant element formulation does not lead to satistactory results in many cases.

Bi-Linear Isoparametric Discontinuous Elements

In this type of boundary element which is used in all CHT calculations, the field variables T and q are modeled with discontinuous bi-linear shape functions across each element while the geometry is represented locally as continuous bi-linear surfaces. Figure A.2 below shows a typical bi-linear subparametric boundary element along with its transformed representation in the local coordinate system.

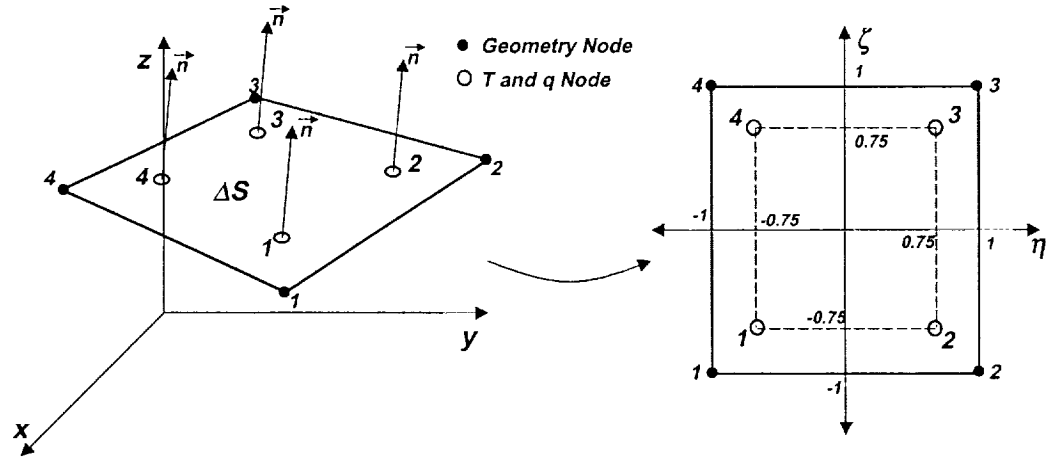

Figure A.2. Bi-linear isoparameteric discontinuous boundary element.

Again, the global coordinate system (x, y, z) is transformed into a local coordinate system (η, ζ) where the four bi-linear shape functions defined in Eq. (A.9). The field variables, T and q, are modeled to vary bi-linearly across the boundary element through the use of four discontinuous shape functions with nodes located at an off-set position of 12.5% from the edges of the element. The field variables and shape functions are described as follows:

$$T^e(\eta,\zeta) = \sum_{j=1}^{4} M_j^e(\eta,\zeta)\, T_j^e \qquad (A.13)$$

$$q^e(\eta,\zeta) = \sum_{j=1}^{4} M_j^e(\eta,\zeta)\, q_j^e$$

with the bilinear shape functions M_j^e defined as,

—

—

—

—

(A.14)

Introducing the above discretization in the BIE in Eq. (A.1), and collocating the discretized BIE at each of the boundary nodes ξ_i there results

$$C(\xi_i)\,T(\xi_i) + \sum_{e=1}^{N}\sum_{j=1}^{NPE} H_{ij}^{e}\,T_j^{e} = \sum_{j=1}^{N}\sum_{j=1}^{NPE} G_{ij}^{e}\,q_j^{e} \tag{A.15}$$

where the influence coefficients H_{ij}^{e} and G_{ij}^{e} are defined as

$$H_{ij}^{e} = \int\int_{\Delta S_j} q^*(x,\xi_i)\,M_j^{e}(\eta,\zeta)\,dS \tag{A.16}$$

$$G_{ij}^{e} = \int\int_{\Delta S_j} T^*(x,\xi_i)\,M_j^{e}(\eta,\zeta)\,dS$$

These influence coefficients are again evaluated numerically via quadratures.

Numerical Evaluation of the Influence Coefficients

The process is illustrated by considering constant elements. Introducing the definition of bilinear representation of the geometry Eq. (A.8) into the constant element influence coefficient definition, Eq. (A.12), the influence coefficient integrals are explicitly,

$$G_{ij} = \int_{-1}^{1}\int_{-1}^{1} q^*(x(\eta,\zeta),\xi_i)|J_j(\eta,\zeta)|\,d\eta\,d\zeta \tag{A.17}$$

$$H_{ij} = \int_{-1}^{1}\int_{-1}^{1} T^*(x(\eta,\zeta),\xi_i)|J_j(\eta,\zeta)|\,d\eta\,d\zeta$$

The Jacobian of the transformation over the j-th element, $|J_j(\eta,\zeta)|$ is

$$J_j(\eta,\zeta) = \sqrt{g_{\eta\eta}g_{\zeta\zeta} - g_{\eta\zeta}^2} \tag{A.18}$$

where $g_{\eta\eta}$, $g_{\zeta\zeta}$, and $g_{\eta\zeta}$ are the components of the metric tensor defined as,

$$\frac{}{} \qquad \frac{}{} \qquad \frac{}{} \tag{A.19}$$

$$\frac{}{} \qquad \frac{}{} \qquad \frac{}{}$$

$$\frac{}{}\frac{}{} \qquad \frac{}{}\frac{}{} \qquad \frac{}{}\frac{}{}$$

The metrics $\frac{\partial x}{\partial \eta}$, $\frac{\partial x}{\partial \zeta}$, $\frac{\partial y}{\partial \eta}$, $\frac{\partial y}{\partial \zeta}$, $\frac{\partial z}{\partial \eta}$, and $\frac{\partial z}{\partial \zeta}$ are readily found by differentiation of $x^e(\eta, \zeta)$, $y^e(\eta, \zeta)$, and $z^e(\eta, \zeta)$ in Eq. (A.8). Introducing the metrics into the Jacobian and simplifying leads to,

$$J_j(\eta,\zeta) = \tag{A.20}$$
$$\sqrt{\left(\frac{\partial y}{\partial \eta}\frac{\partial z}{\partial \zeta} - \frac{\partial z}{\partial \eta}\frac{\partial y}{\partial \zeta}\right)^2 + \left(\frac{\partial z}{\partial \eta}\frac{\partial x}{\partial \zeta} - \frac{\partial x}{\partial \eta}\frac{\partial z}{\partial \zeta}\right)^2 + \left(\frac{\partial x}{\partial \eta}\frac{\partial y}{\partial \zeta} - \frac{\partial y}{\partial \eta}\frac{\partial x}{\partial \zeta}\right)^2}$$

In the expression for $q^*(x, \xi_i)$ there arises the need to evaluate the outward-drawn normal $\widehat{n}$, as by definition

$$q^*(x, \xi_i) = \frac{\partial T^*(x, \xi_i)}{\partial n} = \nabla q^*(x, \xi_i) \cdot \widehat{n} \tag{A.21}$$

The components of the unit vector on each elements can be easily computed using,

$$n_x = \left(\frac{\partial y}{\partial \eta}\frac{\partial z}{\partial \zeta} - \frac{\partial z}{\partial \eta}\frac{\partial y}{\partial \zeta}\right)/J_j(\eta,\zeta) \tag{A.22}$$
$$n_y = \left(\frac{\partial z}{\partial \eta}\frac{\partial x}{\partial \zeta} - \frac{\partial x}{\partial \eta}\frac{\partial z}{\partial \zeta}\right)/J_j(\eta,\zeta)$$
$$n_z = \left(\frac{\partial x}{\partial \eta}\frac{\partial y}{\partial \zeta} - \frac{\partial y}{\partial \eta}\frac{\partial x}{\partial \zeta}\right)/J_j(\eta,\zeta)$$

The numerical integration process necessary to obtain the influence coefficients in Eq. (A.17) is performed by double Gaussian quadratures (Gauss-Legendre specifically) simultaneously along the two local axis η and ζ, leading to the following form,

$$G_{ij} = \sum_{n=1}^{NG}\sum_{m=1}^{NG} W_n W_m E_j(\eta_{nm}, \zeta_{nm}, \xi_i)|J_j(\eta_{nm}, \zeta_{nm})| \tag{A.23}$$
$$H_{ij} = \sum_{n=1}^{NG}\sum_{m=1}^{NG} W_n W_m F_j(\eta_{nm}, \zeta_{nm}, \xi_i)|J_j(\eta_{nm}, \zeta_{nm})|$$

where NG is the number of Gaussian points or order of integration employed, η_{nm} and ζ_{nm} are the locations of the Gaussian quadrature points (zeroes of the appropriate Legendre polynomials), and W_n and W_m are the quadrature weights [1,2].

The number of Gaussian points employed can be addapted to every integral depending of the variability of the integrand. The influence coefficients G are inversly proportional to the Euclidean distance between the field or integration point x and the collocation point ξ_i, and the influence factors H are inversly proportional to the square of the Euclidean distance between the field or integration point and the collocation point ξ_i. Therefore, as the collocation point ξ_i is positioned closer to the integration element, the variability of the integrand increases requiring an increase in the number of Gaussian points, NG, for the integral approximation to provide a similar level of accuracy. Hence, a simple distance rule can be heuristically employed to change the number of Gaussian points depending on how far the collocation point is to the integration element.

However, simply increasing the number of Gaussian integration points is in some cases not enough to obtain an accurate approximation to the integral. This is precisly the case when the collocation point ξ_i is extremely close to the integration element. In such cases a subsegmentation of the element is required and can be performed in a similar fashion as to the increase of Gaussian points, that is, the closer the collocation point is to the element, the more subdivisions are made to the element with a fixed number of Gaussian points for each subelement.

The particular case in which the collocation point ξ_i is located over the integration element must be treated with caution. For this case the integrand becomes singular lacking an accurate integral approximation through a regular Gaussian rule. Even though the integral for the influence factor H_{ii} is strongly singular because its integrand is inversely proportional to the distance squared $(1/r^2)$, this integral need not be computed directly but instead using the equipotential relation by suming the off-diagonal terms[3-5], that is

$$H_{ii} = -\sum_{j=1, j\neq i}^{N} H_{ij} \tag{A.24}$$

The integral for the influence coefficient G_{ii} is however weakly singular because its integrand is inversely proportional to the distance $(1/r)$, therefore the singularity may be avoided through an additional transformation of the local coordinate system. Figure A.3 shows the primary

subsegmentation of the singular element. Twelve (12) quadrilateral subdivisions have been made to the singular subparametric boundary element in Fig. A.3 and ten (10) quadrilateral subdivisions to the singular isoparametric boundary element in Fig. A.4. The shaded area (0) corresponds to the singular portion of the element that is going to be transformed into a local polar coordinate system as shown in Fig. A.5.

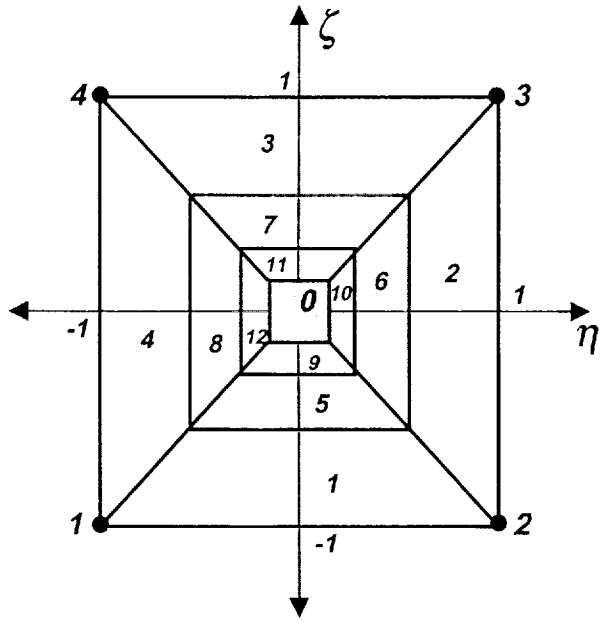

Figure A.3. Subsegmentation of singular bi-linear subparametric boundary element.

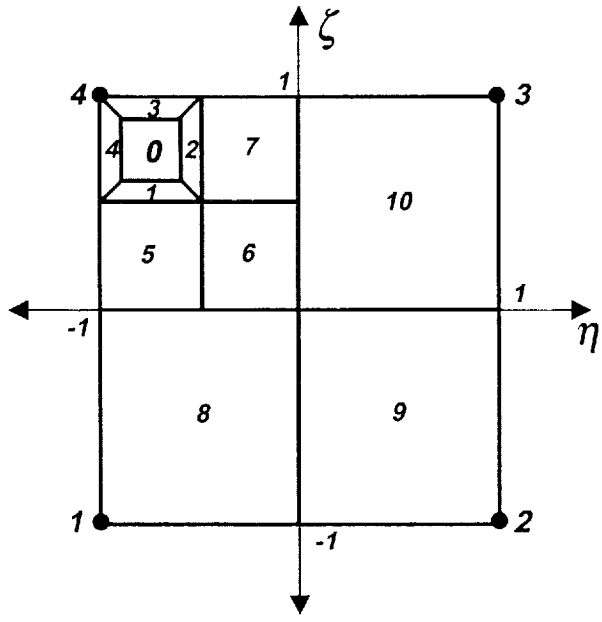

Figure A.4. Sub-segmentation of singular bi-linear isoparametric boundary element.

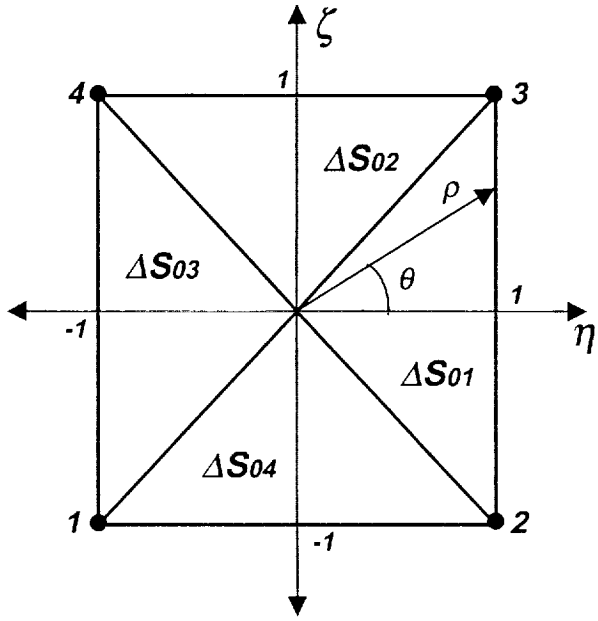

Figure A.5. Polar coordinate transformation of singular boundary element.

The shaded area of the singular element is fit into a new local system (η, ζ) and subdivided into four triangular subelements. Each of the subelements is transformed into a new local polar coordinate system (ρ, θ) where,

$$\begin{aligned} \eta &= \rho \cos\theta \\ \zeta &= \rho \sin\theta \end{aligned} \tag{A.25}$$

therefore, the factor G_{ii}^{0} which corresponds to the integral over the shaded area (0) is comprised of four integrals (G_{ii}^{01}, G_{ii}^{02}, G_{ii}^{03}, and G_{ii}^{04}) as,

$$G_{ii}^{01} = \int_{-\frac{\pi}{4}}^{\frac{\pi}{4}} \int_{0}^{\frac{1}{\cos\theta}} T^{*}(x(\eta,\zeta),\xi_i)|J(\eta,\zeta)|\rho\, d\rho\, d\theta \tag{A.26}$$

$$G_{ii}^{02} = \int_{\frac{\pi}{4}}^{\frac{3\pi}{4}} \int_{0}^{\frac{1}{\sin\theta}} T^{*}(x(\eta,\zeta),\xi_i)|J(\eta,\zeta)|\rho\, d\rho\, d\theta$$

$$G_{ii}^{03} = \int_{\frac{3\pi}{4}}^{\frac{5\pi}{4}} \int_{0}^{\frac{1}{\cos\theta}} T^{*}(x(\eta,\zeta),\xi_i)|J(\eta,\zeta)|\rho\, d\rho\, d\theta$$

$$G_{ii}^{04} = \int_{\frac{5\pi}{4}}^{\frac{7\pi}{4}} \int_{0}^{\frac{1}{\sin\theta}} T^{*}(x(\eta,\zeta),\xi_i)|J(\eta,\zeta)|\rho\, d\rho\, d\theta$$

Notice that the transformation of the differential area introduced the variable ρ to the integrand which relaxes the singularity of the fundamental solution $T^*(x(\eta,\zeta),\xi)$. In addition, an extra transformation is necessary to fit the limits of integration into the $(-1,1)$ range such that,

$$\begin{aligned}
\rho_1 &= \frac{s+1}{2cos\,\theta} \;,\; \theta_1 = \frac{\pi}{4}t \\
\rho_2 &= \frac{s+1}{2sin\,\theta} \;,\; \theta_2 = \frac{\pi}{4}(t+2) \\
\rho_3 &= \frac{s+1}{2cos\,\theta} \;,\; \theta_3 = \frac{\pi}{4}(t+4) \\
\rho_4 &= \frac{s+1}{2sin\,\theta} \;,\; \theta_4 = \frac{\pi}{4}(t+6)
\end{aligned} \tag{A.27}$$

where the sub-indeces of the coordinates ρ and θ correspond to the transformation for the particular integral term G_{ii}^{01}, G_{ii}^{02}, G_{ii}^{03}, and G_{ii}^{04}. Therefore, the influence coefficient subintegrals are transformed into,

$$\begin{aligned}
G_{ii}^{01} &= \int_{-1}^{1}\int_{-1}^{1} T^*(x(\eta,\zeta),\xi_i)|J(\eta,\zeta)|\,\frac{\pi\rho_1}{8cos\,\theta_1}\,ds\,dt \\
G_{ii}^{02} &= \int_{-1}^{1}\int_{-1}^{1} T^*(x(\eta,\zeta),\xi_i)|J(\eta,\zeta)|\,\frac{\pi\rho_2}{8sin\,\theta_2}\,ds\,dt \\
G_{ii}^{03} &= \int_{-1}^{1}\int_{-1}^{1} T^*(x(\eta,\zeta),\xi_i)|J(\eta,\zeta)|\,\frac{\pi\rho_3}{8cos\,\theta_3}\,ds\,dt \\
G_{ii}^{04} &= \int_{-1}^{1}\int_{-1}^{1} T^*(x(\eta,\zeta),\xi_i)|J(\eta,\zeta)|\,\frac{\pi\rho_4}{8sin\,\theta_4}\,ds\,dt
\end{aligned} \tag{A.28}$$

which can be solved numerically by the use of Gaussian integration and through the corresponding transformations detailed in the previous relations.

When dealing with isorparametric bi-linear elements, the procesure of evalaution of the element influence coefficients H_{ij}^{e} and G_{ij}^{e} is the same, except that the shape functions $M_j^e(\eta,\zeta)$ appear multiplying each of the integrands of the influence coefficients, see Eq. (A.16). That is for instance,

$$\begin{aligned}
G_{ij}^{e} &= \int_{-1}^{1}\int_{-1}^{1} q^*(x(\eta,\zeta),\xi_i)M_j^e(\eta,\zeta)|J_e(\eta,\zeta)|\,d\eta\,d\zeta \\
G_{ij}^{e} &= \sum_{n=1}^{NG}\sum_{m=1}^{NG} W_n W_m q_j^*(\eta_{nm},\zeta_{nm},\xi_i)M_j^e(\eta_{nm},\zeta_{nm})|J_e(\eta_{nm},\zeta_{nm})|
\end{aligned} \tag{A.29}$$

where the subscript e is used to denote that the Jacobian is evaluated on an element basis, as in this case $j = 1,2...NPE = 4$. Moreover, the sub-segmentation described for the G_{ij}^{e} is

performed non-symmetrically depending on the location of the collocation point ξ_i on the boundary element "e", see Fig. (A.2).

References

[1] Abramowitz, M. and Stegun, I., Handbook of Mathematical Functions, Dover Publications, New York, 1965.

[2] Ralston, A. and Rabinowitz, P., A First Course in Numerical Analysis, Mc Graw Hill Book Co., New York, 1978.

[3] Brebbia, C.A., Telles, J.C.F. and Wrobel, L.C., *Boundary Element Techniques*, Springer- Verlag, Berlin, 1984.

[4] Kane, J.H., *Boundary Element Analysis in Engineering Continuum Mechanics*, Prentice- Hall, New Jersey, 1993.

[5] Banerjee, P.K., *Boundary Element Method*, MacGraw Hill Book, Co, New York, 1994.